ADVANCED FUNCTIONAL MATERIALS
www.afm-journal.de

Precise p-Type Substitutional Doping Enables WS_2 p-n Anti-Ambipolar Homojunction Phototransistor Arrays

*Boxiang Gao, Yan Yan, Shuai Zhang, Zenghui Wu, You Meng, Yuxuan Zhang, Weijun Wang, Yi Shen, Siliang Hu, Bowen Li, He Shao, Pengshan Xie, SenPo Yip, and Johnny C. Ho**

Van der Waals (vdWs) p–n junctions assembled from 2D materials offer enhanced flexibility for creating versatile electronic and optoelectronic devices, attracting significant interest. However, the lack of reliable methods to produce high-quality p-type 2D semiconductors, especially patterned p-type channels, remains a major challenge for progress in the field. Here, a precise substitutional doping strategy for 2D semiconductors is presented, enabling the production of millimeter-scale WS_2 single-crystal thin films with tailored p-type and n-type properties. This advancement supports the fabrication of high-performance WS_2-based p-type and n-type field-effect transistor (FET) miniaturized arrays with near-ohmic contact. Building on this progress, a WS_2 van der Waals homojunction p-n array demonstrating distinct anti-ambipolar behavior and excellent rectification characteristics is developed. In self-powered photodetection mode, leveraging the strong coupling of the vdWs homojunction interface, the device achieves an exceptional photovoltaic effect with a high specific detectivity of 3.4×10^{10} Jones and a fast response time of 400 µs. The development of WS_2 p-n homojunction arrays presents immense potential for advancing next-generation logic electronics and optoelectronic devices, opening new avenues for large-scale industrial applications.

1. Introduction

Layered 2D semiconductors, with their atomic-scale thickness, have emerged as promising candidates for extending Moore's Law.[1–3] Their unique properties, particularly the flexibility to assemble through van der Waals (vdWs) stacking without reliance on chemical bonding or lattice matching constraints, create new opportunities for designing and developing multifunctional electronic devices.[4–9] This flexibility is well demonstrated by anti-ambipolar transistors based on the series integration of p-type and n-type 2D field-effect transistor (FET) channel materials.[10–12] These transistors exhibit distinctive differential transconductance (or resistance) behavior under both positive and negative gate biases, showcasing their potential for simplifying circuit design and reducing power consumption.[13–15] Their gate-tunable rectification properties are ideal for developing rectifiers and photodiodes.[16–18] Currently, the advancement of n-type 2D FETs based on transition metal dichalcogenides (TMDs), such as MoS_2 and WS_2, has steadily progressed toward fulfilling the performance benchmarks established in the international roadmap for devices and systems.[19,20] However, the scarcity of intrinsically p-type TMD semiconductors has become a major bottleneck,[21] significantly limiting the broader development and adoption of 2D anti-ambipolar phototransistor devices.

Doping, the deliberate introduction of specific impurity atoms with precisely controlled concentrations, is a cornerstone for tuning semiconductor properties and enabling device fabrication. Unfortunately, ion implantation, a key doping technique for silicon-based semiconductors, does not apply to 2D materials despite its precision in creating p-type and n-type regions.[22] Substitutional doping offers a stable and dependable method for modifying the electrical properties of 2D materials.[23–25] Incorporating metal dopants, such as V,[24] Nb,[23,24] or Re,[26] as well as non-metal dopants like C,[27] N,[28] or O,[29,30] into the lattice of TMDs, where they substitute transition metal atoms or chalcogen elements respectively, enables modulation of the intrinsic electrical polarity and carrier type of TMDs materials. Nevertheless, it remains to be determined whether these materials fulfill application requirements and can be effectively integrated into industrial production lines, either at the front-end or back-end, through homo- or hetero-integration technologies. Achieving this goal requires overcoming several challenges, including the large-area

B. Gao, Y. Yan, S. Zhang, Z. Wu, Y. Meng, Y. Zhang, W. Wang, Y. Shen, S. Hu, B. Li, H. Shao, P. Xie, J. C. Ho
Department of Materials Science and Engineering
City University of Hong Kong
Hong Kong, SAR 999077, China
E-mail: johnnyho@cityu.edu.hk

S. Yip, J. C. Ho
Institute for Materials Chemistry and Engineering
Kyushu University
Fukuoka 816–8580, Japan

J. C. Ho
State Key Laboratory of Terahertz and Millimeter Waves
City University of Hong Kong
Hong Kong, SAR 999077, China

The ORCID identification number(s) for the author(s) of this article can be found under https://doi.org/10.1002/adfm.202425884

DOI: 10.1002/adfm.202425884

growth of uniform 2D p-type and n-type TMD films with controllable doping schemes, the fabrication of patterned p-type and n-type channels, the reduction of interface contact resistance (R_C), and the development of damage-free transfer processes for vdWs stacking.[31,32]

In this work, we successfully synthesized millimeter-scale monolayer vanadium (V)-doped WS_2 single crystal thin films as p-type channel materials through an atomic substitution doping strategy to introduce hole carriers combined with a liquid-phase-assisted chemical vapor deposition (CVD) technique. By aligning the work function, nickel (Ni) was employed as the contact electrode, achieving an ultra-low interface contact barrier of only 22 meV. This facilitated the development of high-performance 2D p-type FETs with an unprecedented on/off current ratio exceeding 10^6. Furthermore, quasi-ohmic contact p-type and n-type FET arrays based on WS_2 were constructed, demonstrating significant potential for large-scale industrial production of advanced electronic devices. Building on these advancements, we developed an anti-ambipolar phototransistor array based on the WS_2 p-n vdWs homojunction, utilizing patterned film transfer and a precise alignment process. When operated as a back-gate FET, the device exhibited pronounced anti-ambipolar characteristics under gate voltage modulation, attributed to variations in series resistance. This distinct behavior underscores its potential for integration into high-performance logic circuits. In addition, as a photodiode, the device harnessed the built-in electric field (E_{in}) at the WS_2 p-n junction interface to achieve excellent rectification properties, ultra-low reverse dark currents in the sub-picoampere range, and photovoltaic characteristics. Under zero-bias conditions, the photodiode demonstrated a photocurrent on/off ratio of $\approx 10^3$ for visible light detection, a high specific detectivity of 3.4×10^{10} Jones, and a fast response time of 400 µs. These capabilities are attributed to the strong coupling and defect-free nature of the vdWs homojunction interface. These outstanding properties highlight the versatility of WS_2-based p-n homojunction structures, presenting a transformative pathway for designing multifunctional devices and advancing next-generation electronics and optoelectronics for large-scale industrial implementation.

2. Results and Discussion

2.1. Large-Size Monolayer Pristine and V-Doped WS_2 Single-Crystal Thin Films

In our previous study, we developed a liquid-phase precursor approach that enabled precise control of the V-atom doping ratio within the WS_2 lattice. Notably, when the V doping ratio reached ≈5%, the WS_2 thin films exhibited excellent p-type semiconductor behavior.[33] Building upon it, we further enhanced the method by incorporating iodixanol solution as a medium to blend the precursor, optimizing the spin-casting process effectively. This refinement enabled the successful fabrication of millimeter-scale monolayer p-type V-doped and n-type pristine WS_2 single crystals using a liquid-phase precursor-assisted CVD method. The schematic of the CVD growth system is shown in Figure S1 (Supporting Information).

Figure 1a shows an optical microscopy (OM) image of the as-grown, large-size monolayer pristine WS_2, with single-crystal domains extending beyond 600 µm in edge length. The high-angle annular dark-field scanning transmission electron microscopy (HAADF-STEM) image (Figure 1b) reveals a characteristic hexagonal lattice structure, displaying the alternating arrangement of W and S atoms. This lattice configuration is further confirmed by selected area electron diffraction (SAED) analysis, with intensity profiles indicating an interatomic W-W distance of 3.18 Å (Figure 1c). The Raman spectrum of the large-size domain (under 532 nm excitation, Figure 1d) exhibits the characteristic peaks of monolayer WS_2, with the E_{2g} and A_{1g} vibrational modes appearing at 350 and 417 cm^{-1}, respectively. The fabrication of monolayer p-type WS_2 with V atoms as the dopant has also been successfully achieved, with the crystal domain size remarkably exceeding 1000 µm (Figure 1e). The corresponding HAADF-STEM image is shown in Figure 1f, where V atoms are directly observed within the hexagonal lattice by their dimmer contrast as their lower atomic number. In the lattice, V atoms randomly and uniformly substitute some of the W atoms as dopants, with the distance between adjacent metal atoms measured to be 3.20 Å (Figure 1g). The energy dispersive X-ray spectroscopy (EDS) mapping images demonstrate the successful incorporation of V atoms into WS_2 and their uniform distribution within the lattice (Figure S2, Supporting Information), and the statistical analysis reveals that the V atoms doping ratio is 5.02% (Figure S3, Supporting Information). The Raman spectrum of the V-doped WS_2 thin film retains the characteristic E_{2g} and A_{1g} peaks of monolayer WS_2 (Figure 1h). Remarkably, compared to pristine WS_2, the E_{2g} peak exhibits a significant reduction in intensity, accompanied by a blueshift in its position (Figure S4, Supporting Information). These changes are attributed to lattice disorder induced by V atoms and the introduction of holes due to V acting as p-type dopants.[34–36] For the same reason, the pristine WS_2 monolayer exhibits a strong photoluminescence (PL) peak at 1.94 eV. At the same time, the V-doped WS_2 shows a redshift of 80 meV in its PL peak (Figure 1i), accompanied by a broadening and a reduction in intensity.[36] The spectral mapping images (E_{2g} peak, A_{1g} peak, E_{2g}/A_{1g} intensity ratio, and PL peak) for both monolayer pristine and V-doped WS_2, as shown in Figure S5 (Supporting Information), exhibit consistent intensity signals across the entire crystal domains. This uniformity highlights V dopants' successful and homogeneous incorporation within the WS_2 lattice. The X-ray photoelectron spectroscopy (XPS) of W 4f core level peaks exhibit a shift of ≈0.7 eV to lower binding energies in the $4f_{7/2}$ (32.5 eV) and $4f_{5/2}$ (34.6 eV) peaks of the V-doped WS_2, compared to the $4f_{7/2}$ (33.2 eV) and $4f_{5/2}$ (35.3 eV) peaks observed in pristine WS_2 (Figure 1j), indicating a downward shift of the Fermi level attributable to p-type doping.[23,37]

Accurate quantification of the band structure in doped systems is essential for advancing device-level engineering. To address this, the electronic structure of V-doped WS_2 thin films was identified by UV photoelectron spectroscopy (UPS). The energy gap (E_{VB}) between the Fermi level and the valence band maximum (VBM) for V-doped WS_2 was directly measured from the valence band region using the linear intersection method, yielding a value of 0.73 eV (Figure 1k). The work function (equivalent to the Fermi level, E_F) was determined from the secondary

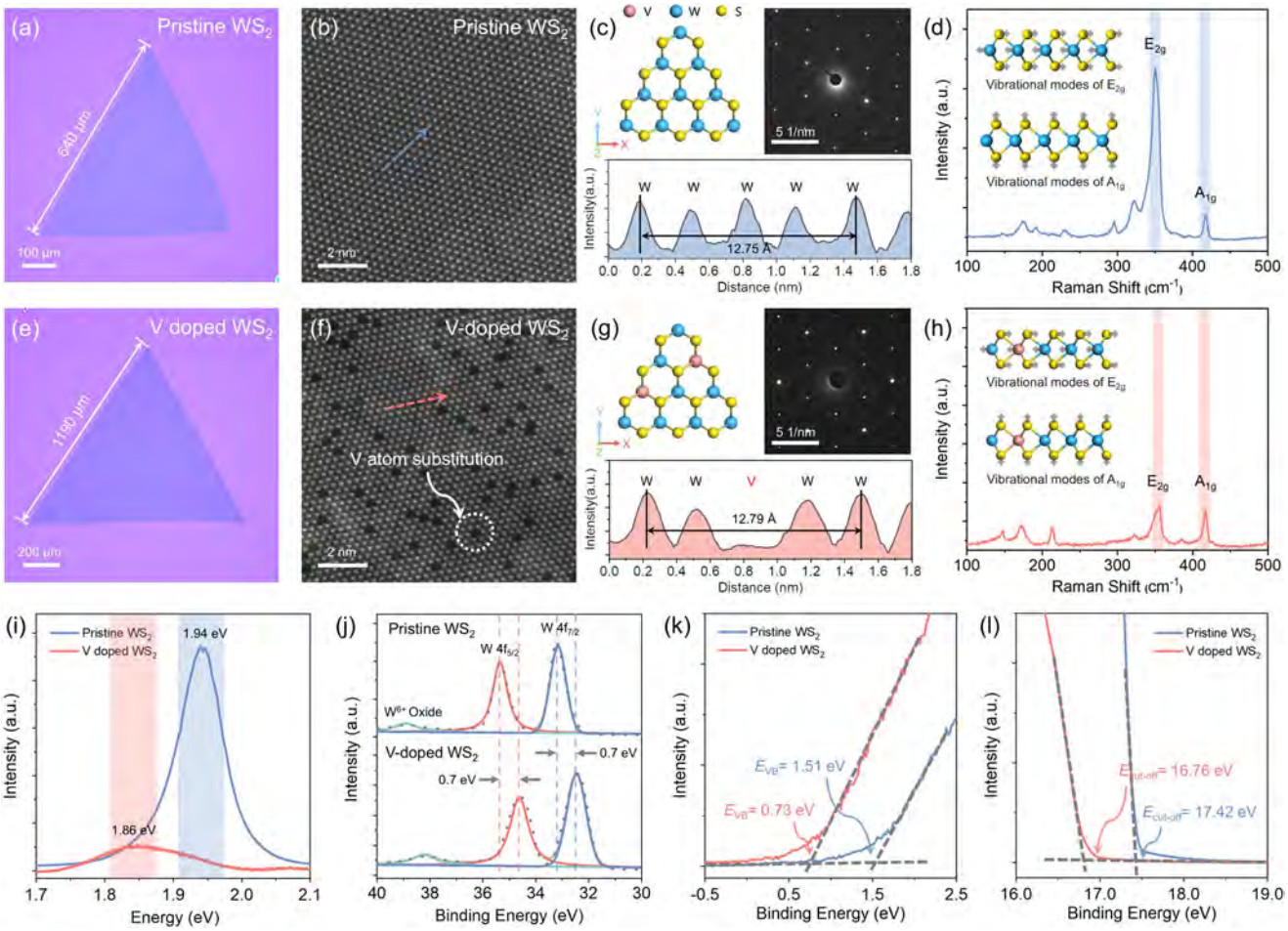

Figure 1. Characterizations of large-size monolayer pristine and V-doped WS_2. a) Typical OM image of as-grown large-size monolayer pristine WS_2 on a SiO_2(270 nm)/Si substrate. b) HAADF-STEM image of monolayer pristine WS_2. c) Structural model, a SAED diffraction pattern (top) of pristine WS_2, and intensity profile (bottom) along the dashed arrow indicated in Figure 1b. d) Raman spectrum of monolayer pristine WS_2, with insets showing the corresponding E_{2g} and A_{1g} vibration modes. e) OM image of as-grown large-size monolayer V-doped WS_2. f) HAADF-STEM image of V-doped WS_2. g) Structural model, a SAED diffraction pattern (top) of V-doped WS_2, and intensity profile (bottom) along the dashed arrow indicated in Figure 1f. h) Raman spectrum of V-doped WS_2, with insets showing the corresponding E_{2g} and A_{1g} vibration modes. i,j). PL spectra (i) and XPS spectra of the W 4f core level peak regions (j) for monolayer pristine and V-doped WS_2. k,l) UPS spectra of monolayer pristine and V-doped WS_2 at valence-band regions (k) and secondary electron cut-off regions (l).

electron cut-off region shown in Figure 1l. The E_F of V-doped WS_2 was calculated to be 4.46 eV (vs vacuum level) using the formula $E_F = h\nu - E_{cut\text{-}off}$, where the excitation energy for He I was 21.22 eV. Similarly, for pristine WS_2, the E_{VB} was determined to be 1.51 eV, and the E_F was 3.80 eV. The optical bandgap (E_g) was obtained from the PL measurements shown in Figure 1i. Based on these results, the positions of the VBM and conduction band minimum (CBM) were established, and the energy band alignment between the V-doped and pristine WS_2 is effectively illustrated ($E_{VBM} = E_F + E_{VB}$ and $E_{CBM}(\chi) = E_F + E_{VB} - E_g$), as shown in Figure S6 (Supporting Information). For pristine WS_2, the Fermi level resides distinctly above the mid-gap, reflecting its intrinsic n-type electronic properties. In contrast, V doping at a ratio of 5.02% introduces a substantial number of holes into the WS_2 lattice, shifting the Fermi level closer to the VBM, accompanied by slight upward shifts in the positions of the VBM and CBM levels. Consequently, the Fermi level drops below the mid-gap, indicating a clear p-type electronic characteristic for the V-doped WS_2.

2.2. Patterning of WS_2 for p- and n-Type FET Arrays with Quasi-Ohmic Contact

The successful fabrication of large-size monolayer V-doped, and pristine WS_2 single-crystal domains has laid a solid foundation for achieving patterned homogeneous p-type and n-type channels in integrated circuits. However, the high electrical R_C in WS_2-based FETs currently hinders further technological advancements. As for the interface R_C of p-type V-doped WS_2, no reports of this kind have been documented to date. In principle, the R_C at the metal-semiconductor interface is governed by two key factors: (I) the energy band alignment between the metal and the semiconductor, where the metal work function (Φ_m) plays a

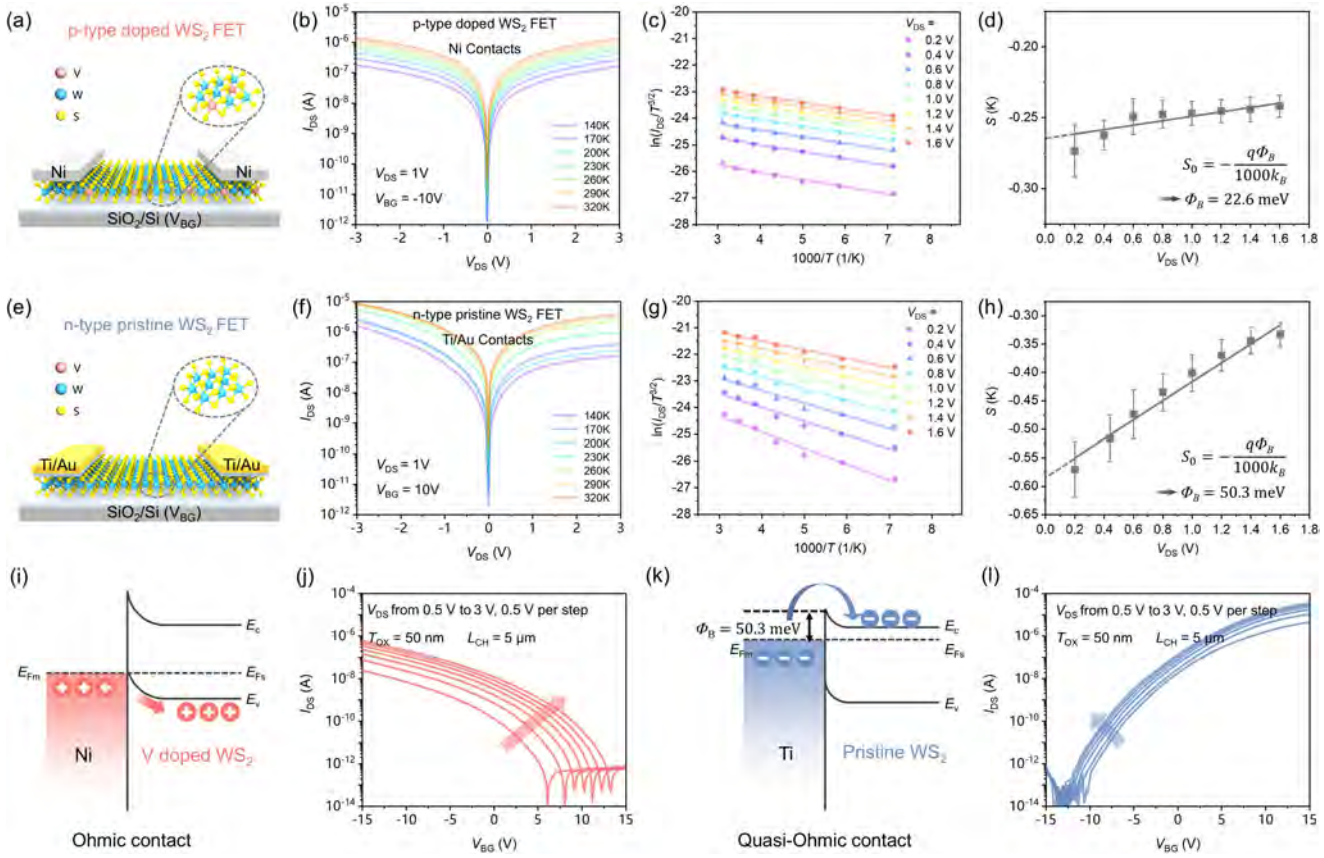

Figure 2. Metal-semiconductor interface contact barrier height of V-doped and pristine monolayer WS_2. a) Schematic of a back-gated p-type V-doped WS_2 FET device with Ni contact electrodes. b) I_{DS}-V_{DS} output characteristics of the p-type doped WS_2 FET with Ni contacts at various temperatures. c) Linear fit of the Arrhenius plot, ln ($I_{DS}/T^{3/2}$) versus 1000/T under various bias voltage. d) Slopes extracted from Figure 2c as a function of V_{DS}, with the barrier height (Φ_B) determined from the y-intercept, S_0. e) Schematic of a back-gated n-type pristine WS_2 FET device with Ti/Au contact electrodes. f) I_{DS}-V_{DS} output characteristics of the n-type pristine WS_2 FET. g) Linear fit of the Arrhenius plot, ln ($I_{DS}/T^{3/2}$) versus 1000/T. h) Slopes extracted from Figure 2g as a function of V_{DS}. i) Band diagram of p-type V-doped WS_2 with Ni contacts, showing the formation of an ohmic junction. j) Transfer characteristics of p-type V-doped WS_2 FET with Ni contacts measured at ambient temperature. k) Band diagram of n-type pristine WS_2 with Ti/Au contacts, illustrating a quasi-ohmic junction with an extremely low SBH. l) Transfer characteristics of the n-type pristine WS_2 FET with Ti/Au contacts.

critical role in determining the Schottky barrier height;[38,39] and (II) the density of defects introduced during the metal deposition process, which exacerbate Fermi level pinning.[40,41] A comprehensive understanding of these mechanisms provides valuable insights into strategies for reducing contact resistance and optimizing the performance of WS_2-based electronic devices.[42]

Drawing on the experimentally obtained band structure (Figure S6, Supporting Information), for p-type V-doped WS_2, the E_F is located 4.46 eV below the vacuum level (E_{vac}) and 3.80 eV for n-type pristine WS_2, nickel (Ni, Φ_{Ni} = 5.15 eV) and titanium (Ti, Φ_{Ti} = 4.33 eV) were strategically chosen as contact electrodes for V-doped and pristine WS_2 FETs, respectively. This selection balances cost efficiency considerations, industrial fabrication scalability, and the optimization of electron affinity alignment between the metals and semiconductors. In our experiment, all the contact electrodes are fabricated using a deposition method, with the metal deposition rate carefully controlled at a low level to prevent Fermi-level pinning caused by film damage. In an ideal scenario, for p-type V-doped WS_2, Ni metal has a higher electron affinity, causing electrons to transfer from V-doped WS_2 to the Ni electrode at the interface. This results in the energy bands of V-doped WS_2 bending upward near the interface, forming a p-type anti-Schottky barrier that facilitates hole transport between the metal and semiconductor, thereby establishing an ideal ohmic contact (Figure S7, Supporting Information). In contrast, for n-type pristine WS_2, Ti metal, with a relatively higher electron affinity, also causes the energy bands to bend upward, forming a depletion region at the interface. This generates a Schottky barrier that obstructs electron transport (Figure S8, Supporting Information). Since the electron affinity difference between the Ti metal and the semiconductor is relatively small (Φ_{Ti} – E_F = 0.53 eV), the resulting Schottky barrier is typically low, leading to a quasi-ohmic contact effect.

To prove this hypothesis, FETs with Ni-contacted V-doped WS_2 and Ti/Au-contacted pristine WS_2 were fabricated, each with a channel length of 5 μm. The schematic structures of these devices are illustrated in **Figure** 2a,e. The electrical transport through the metal-semiconductor interface barrier into WS_2 can be elucidated using the 2D thermionic emission equation.[43]

$$I_{DS} = AA^*_{2D}T^{3/2}exp\left[-\frac{q}{k_BT}\left(\Phi_B - \frac{v_{DS}}{n}\right)\right] \quad (1)$$

Here, A represents the contact area of the junction, A^*_{2D} is the Richardson constant, q is the magnitude of the electron charge, Φ_B denotes the Schottky barrier height (SBH), k_B is the Boltzmann constant, and n is the ideality factor. For $qV_{DS} \gg k_BT$, the equation can be simplified as:[44]

$$I_{DS} = A^*_{2D} T^{3/2} exp\left(-\frac{q\Phi}{k_B T}\right) \quad (2)$$

Figure 2b displays the I_{DS}-V_{DS} output characteristics of the p-type V-doped WS_2 FET device at various temperatures ranging from 140 to 320 K with an interval of 30 K, plotted on a logarithmic scale ($V_{BG} = -10$ V). To extract Φ_B, ln ($I_{DS}/T^{3/2}$) is plotted against $1000/T$ for various V_{DS} biases, as shown in Figure 2c, and the data exhibits a linear trend for each bias. Their slope (S) is plotted as a function of $V_{DS,}$ and the calculated Φ_B for the p-type V-doped WS_2 FET with Ti contacts is plotted in Figure 2d. The y-intercept of this plot, labeled as S_0, yields the value of Φ_B according to the equation: $S_0 = -qk_B/1000\Phi_B$, Φ_B is determined to be 22.6 meV under the device's ON-state. Using the same method, the barrier height between Ti/Au electrodes and n-type pristine WS_2 is calculated to be only 50.3 meV (with 10 V bias voltage, Figure 2f–h). Furthermore, the corresponding barrier heights under flat-band conditions were determined at various $V_{BG,}$ as presented in Figure S9 (Supporting Information), resulting in values of 52.2 meV for the Ni/p-type doped WS_2 interface and 82.8 meV for the Ti/Au/n-type pristine WS_2 interface. Additionally, to extract the metal-semiconductor R_C via the transfer line method (TLM), multiple FETs were fabricated on the same p-type doped WS_2 single-crystal domain (Figure S10, Supporting Information). These devices featured a uniform channel width (W_{CH} = 50 μm) and varying channel lengths (L_{CH}) of 2, 4, 6, and 8 μm. The corresponding I_{DS}-V_{BG} transfer curves for different L_{CH} are presented in Figure S11a,b (Supporting Information), plotted on both linear and logarithmic scales. The total resistance (R_{Total}) was extracted from $V_{DS} = 1.0$ V and $V_{BG} = -15$ V; its dependence on L_{CH} is shown in Figure S11c (Supporting Information). By performing linear fitting and extrapolating to the y-axis intercept, the extracted value corresponds to twice the contact resistance ($2R_C$). Consequently, the R_C at the interface was determined to be 1.61×10^6 Ω μm, while the sheet resistance (R_{doped}) was 8.54×10^6 Ω μm^{-1}, as obtained from the TLM analysis. Following the same methodology, the contact resistance at the Ti/Au–n-type pristine WS_2 interface was measured to be 2.01×10^6 Ω μm, with a corresponding sheet resistance ($R_{pristine}$) of 4.66×10^6 Ω μm^{-1} (Figure S11d–f, Supporting Information).

For metal-2D semiconductor interfaces, the aforementioned contact barrier results are considered near-ideal. Figure 2i,k show the energy band diagram at the metal-semiconductor interface. This excellent contact quality between the electrodes and channel materials is directly reflected in the performance of the corresponding FET devices. Specifically, the FET with a p-type V-doped WS_2 channel exhibits an ON/OFF current ratio exceeding 10^6 (Figure 2j), while greater than 10^8 for the FET with an n-type pristine WS_2 channel (Figure 2l). Their corresponding I_{DS}-V_{DS} curves exhibit linear and symmetric characteristics in the low source-drain bias range, further demonstrating the formation of effective quasi-ohmic contacts (Figure S12, Supporting Information).

Precisely fabricating patterned p-type and n-type semiconductors is crucial to realizing integrated circuits. This study successfully patterned millimeter-scale V-doped WS_2 and pristine WS_2 single-crystal domains using the well-established photolithography and physical etching techniques (**Figure 3a** and Experimental Section). The OM images in Figure 3b,c shows the 4 × 4 microrectangular arrays of patterned V-doped and pristine WS_2 thin films (each unit measuring 20×40 μm^2), respectively. The quality of the patterned thin films was evaluated through spectral mapping. As shown in Figure 3d for V-doped and Figure 3e for pristine WS_2, the results reveal strong characteristic signals and excellent uniformity of the arrays, indicating that the optical properties of films can be well preserved.

The successful patterning of WS_2-based channel materials enables the fabrication of FET arrays. As shown in Figure 3f,g, 4 × 4 p-type V-doped WS_2 FETs with Ni contacts and 4 × 4 n-type pristine WS_2 FETs with Ti/Au contacts were fabricated, each with a channel length of 5 μm. The transfer characteristics of these two types of 4 × 4 FET arrays at a bias voltage of 0.5 V are presented in Figure 3h,i, respectively. Benefiting from the prepared millimeter-scale single-crystal domains, the channel materials in the FET array originate from the same domain, completely eliminating the influence of grain boundaries (Figure S13, Supporting Information). This ensures highly consistent transfer characteristics across the FET array units. Their carrier mobilities (μ) were extracted from the corresponding transfer curves using the following formulas[45,46] to generate heatmaps, as shown in Figure 3j,k, respectively,

$$\mu = \frac{L}{WC_iV_{DS}}\frac{dI_{DS}}{dV_{BG}} \quad (3)$$

where C_i is the gate oxide capacitance (69 nF cm^{-2} for a 50-nm-thick SiO_2 dielectric layer), and L and W are the length and width of the channel. The average and maximum mobilities for the p-type V-doped WS_2 FET devices were 0.04 and 0.08 cm^2 V^{-1} s^{-1}, while those for the n-type pristine WS_2 FET devices were 0.5 and 1.6 cm^2 V^{-1} s^{-1}, respectively. Compared to pristine WS_2, the relatively low carrier mobilities in V-doped WS_2 may be attributed to the high-density impurity scattering introduced by the lattice-doped V atoms.[47]

2.3. WS_2 p-n Anti-Ambipolar vdWs Homojunction Phototransistor Arrays

Well-prepared p-type and n-type WS_2 FET arrays enable the p-n homojunction phototransistor fabrication. By employing an established transfer process for 2D materials (**Figure 4a** and Experimental Section), spin-coated PMMA was used as the transfer medium to precisely delaminate the patterned pristine WS_2 arrays from the growth substrate. The arrays were then meticulously aligned under a microscope with the pre-patterned V-doped WS_2 thin films. OM image in Figure 4b illustrates the constructed 2 × 5 WS_2-based p-n homojunction arrays with varying junction widths, demonstrating the excellent editability and flexibility of this approach. Furthermore, the structural integrity of the transferred thin films was well-preserved (Figure 4c; Figure S14, Supporting Information), underscoring the reliability of the

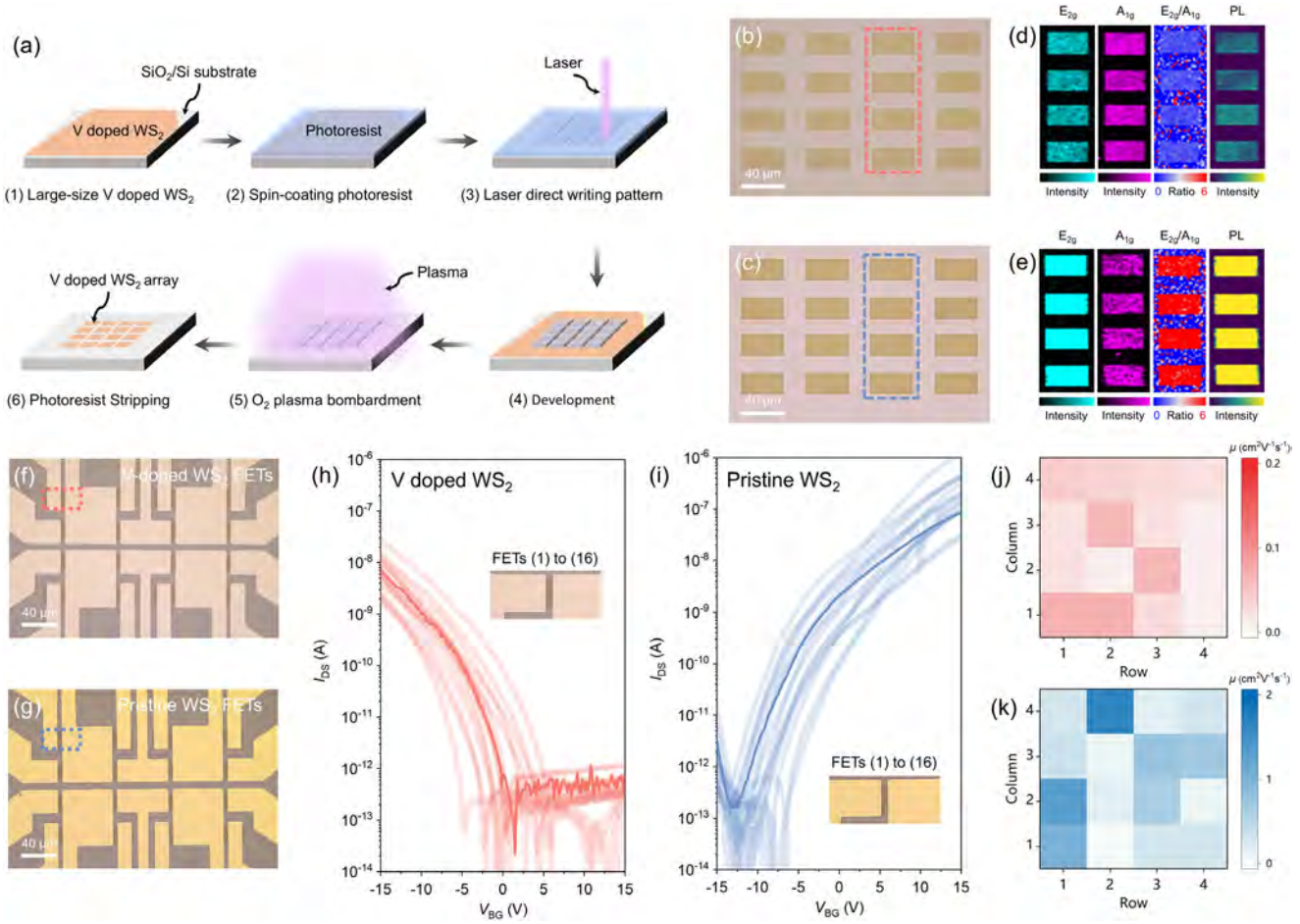

Figure 3. Patterned 4 × 4 arrays of V-doped and pristine WS_2 FETs with quasi-ohmic contacts. a) Schematic illustration of the patterning process for large-size V-doped WS_2. b,c) OM images of the patterned V-doped WS_2 array (b) and the patterned pristine WS_2 array (c) on SiO_2 (50 nm)/Si substrates. d) Spectral mapping images for the Raman E_{2g} peak, A_{1g} peak, E_{2g}/A_{1g} intensity ratio, and PL peak (from left to right) were obtained from the highlighted red box area in Figure 3b. e) Spectral mapping images were obtained from the highlighted blue box area in Figure 3c. f,g) 4 × 4 Arrays of V-doped WS_2 FETs with Ni contact (f) and pristine WS_2 FETs with Ti/Au contact (g). h,i) Transfer characteristics of the V-doped p-type WS_2 (h) and pristine n-type WS_2 (i) FETs array from device 1 to 16 under a 0.5 V bias voltage. j,k). Carrier mobility statistics heatmaps of p-type V-doped WS_2 (j) and n-type pristine WS_2 (k) FET arrays extracted from Figure 3h,i, respectively.

experimental process. The constructed WS_2-based p-n homojunction was characterized using Raman and PL spectroscopy. The Raman mapping image (Figure 4d) of the E_{2g}/A_{1g} intensity ratio clearly distinguishes the p-type, n-type, and homojunction regions with well-defined boundaries. As mentioned earlier, V atom doping weakens the E_{2g} vibrational modes within the lattice and leads to a blueshift of the peak position. In the homojunction region, the E_{2g} characteristic peak reflects the combined influence of V-doped and pristine WS_2 (Figure 4e). Moreover, the PL characteristic peaks in the corresponding homojunction regions also exhibit shifts with the peak at 1.91 eV (Figure S15, Supporting Information).

To investigate the potential ambipolar characteristics under gate voltage modulation of WS_2-based homojunction and their performance as photodetectors, the homojunction array was selected to construct phototransistors with every unit device comprising a p-type channel (electrode (1) and (2), V-doped WS_2, Ni contact), a p-n homojunction channel (electrode (2) and (3), Ni & Ti/Au asymmetric contact), and a n-type channel (electrode (3) and (4), pristine WS_2, Ti/Au contact), as illustrated in Figure 4f. The transfer characteristics reveal that when the V_{BG} is above −12 V, the n-type channel is on-state, while at a V_{BG} below 5 V, the p-type channel transitions into the on-state (Figure 4g). Within the V_{BG} range of −8–5 V, the homojunction demonstrates the ability to transport both electrons and holes, with the type of injected carriers determined by the applied gate voltage. Consequently, the transfer curve exhibits a distinct anti-ambipolar "Λ" shaped pattern (Figure 4h; Figure S16, Supporting Information), achieving a transition between n-type and p-type characteristics at specific gate voltages. Figure 4i–k presents the time-resolved photocurrent characteristics of the three kinds of phototransistors (p-type, homojunction, and n-type channel, respectively) under 1 Hz chopped 532 nm illumination with different back-gate voltage, demonstrating the effective modulation of their photoresponse by the applied back-gate voltage.

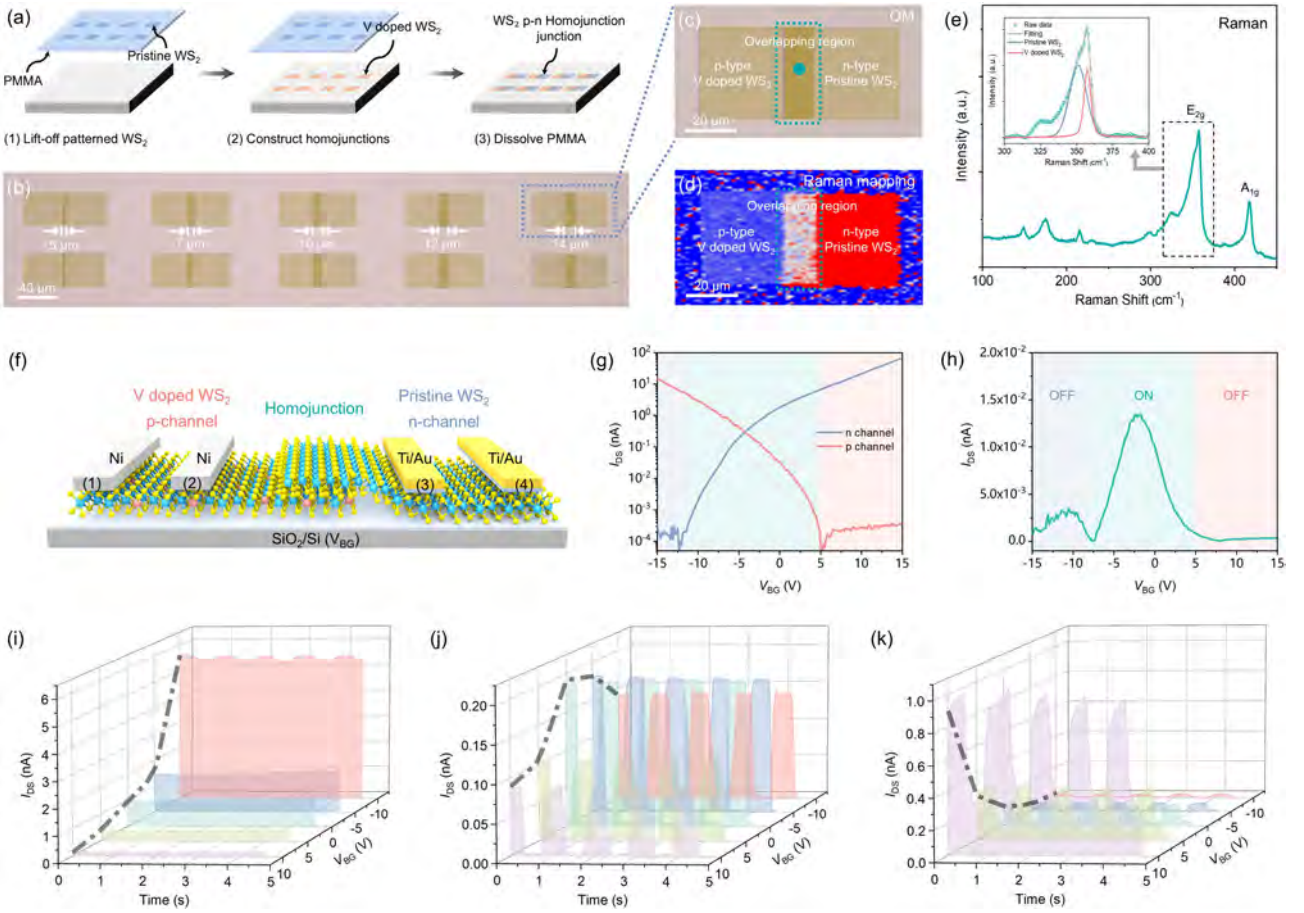

Figure 4. WS_2 anti-ambipolar p-n homojunction phototransistor array. a) Schematic illustration of the transfer process for constructing the WS_2 p-n homojunction array. b) OM image of the WS_2 p-n homojunction array with customizable junction widths. c,d) Zoom-in OM image (c) and E_{2g}/A_{1g} ratio Raman mapping image (d) of a WS_2 p-n homojunction obtained from the blue box area in Figure 4b. e) Raman spectrum of the point at the junction region is shown in Figure 4c. The inset shows the E_{2g} peak fitting details. f) Schematic of the WS_2 p-n homojunction phototransistor device in which the p-type V-doped WS_2 (contact electrode (1) and (2)), the p-n homojunction (contact electrode (2) and (3)) as well as the n-type pristine WS_2 (contact electrode (3) and (4)), serves as the transport channel, respectively. g) Transfer characteristics of the p-type and n-type channel under a 1 V bias. h) Anti-ambipolar characteristics of the WS_2 p-n homojunction channel under a 1 V bias. i–k) Time-dependent photoresponse curves of the p-type V-doped WS_2 (i), p-n homojunction (j), and n-type pristine WS_2 (k) phototransistors at 1 V bias voltage under 532 nm laser with different back-gate voltage.

Meanwhile, the WS_2 p-n homojunction array with quasi-ohmic contacts can function as photodiodes, as depicted in **Figure 5a**, which presents its electrical configuration (top) and structural schematic (bottom). Figure 5b presents its output curves under dark conditions and 532 nm laser illumination (laser density: 6.1 mW cm^{-2}). The V_{DS} ranges from −5 to 5 V with a logarithmic scale and −1.2–1.2 V with a linear scale on the y-axis. The curves exhibit a distinct rectification effect. Under dark conditions, the I_{DS} increases significantly only when a forward V_{DS} is applied while remaining in an off-state under reverse V_{DS}. Due to the quasi-ohmic contacts formed by Ni and Ti/Au as metal electrodes, the metal-semiconductor interface barrier can be neglected. Thus, the asymmetric output curves primarily arise from the built-in electric field generated by the potential difference between the V-doped WS_2 and pristine WS_2 in the junction region, and its direction points from pristine WS_2 to V-doped WS_2 (Figure S17, Supporting Information). Under 532 nm laser illumination, the curve exhibits an obvious short-circuit current (I_{SC}) and an open-circuit voltage (V_{OC}) of 0.12 eV, confirming the photovoltaic behavior of the homojunction structure, which is attributed to the migration of photogenerated electrons and holes driven by the built-in electric field. Figure 5c presents the time-resolved rectification characteristics under a 1 V bidirectional bias with 532 nm laser illumination. The difference in the on-state current of the homojunction is attributed to the distinct carrier dynamics under different bias directions (Figure 5d). Under forward bias, the applied electric field weakens the built-in field, narrowing the depletion region and allowing majority carriers to more readily overcome the p-n junction barrier, resulting in a forward current. The total current is the superposition of the forward and photogenerated currents. Conversely, under reverse bias, the applied electric field strengthens the built-in field, widening the depletion region and hindering the diffusion of majority carriers. In this case, the current primarily arises from the migration of minority and photogenerated carriers.

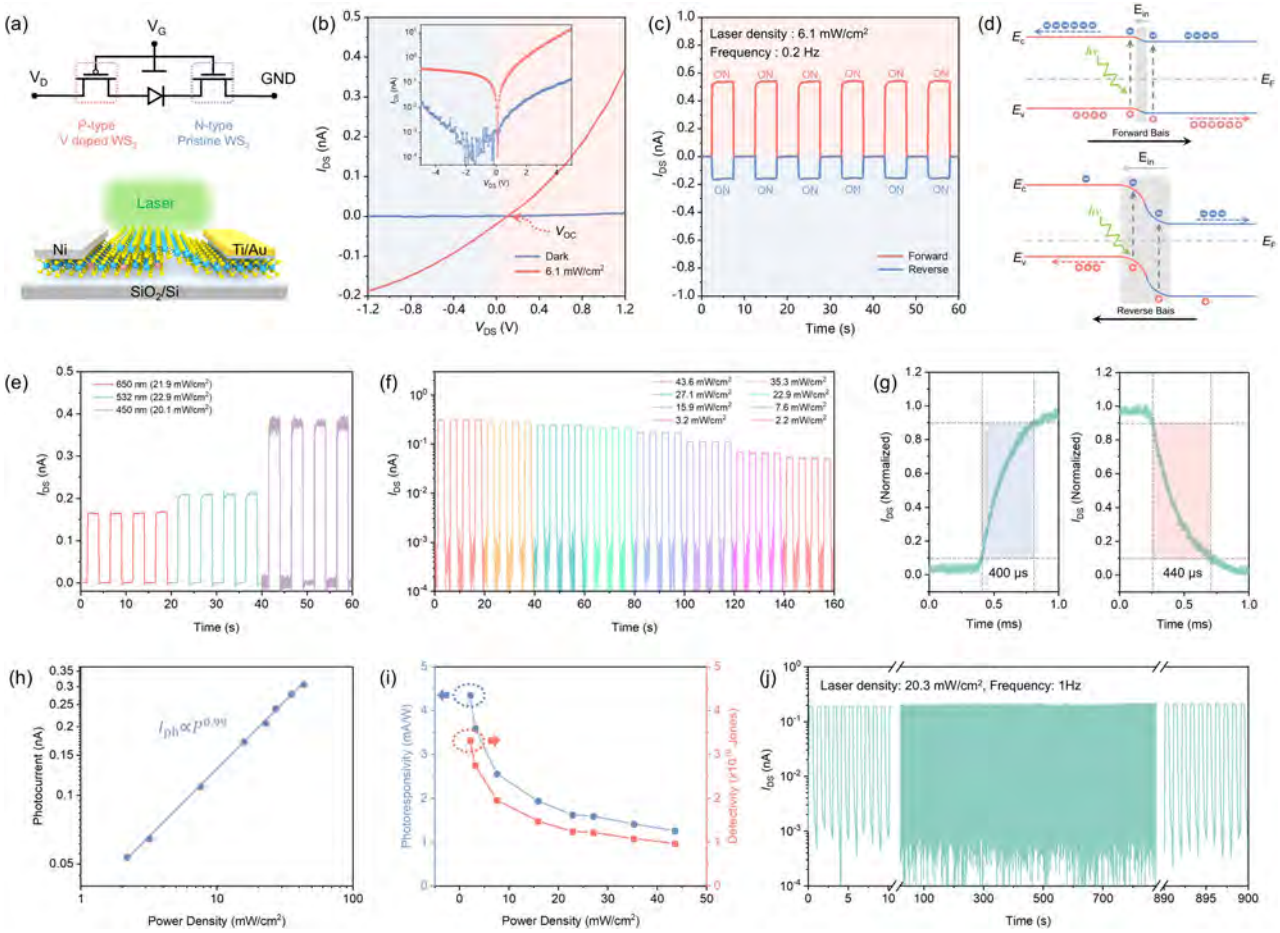

Figure 5. Self-driven WS_2 p-n homojunction photodiode. a) Electrical configuration (top) and schematic illustration (bottom) of the WS_2 p-n homojunction photodiode with quasi-ohmic contacts. b) Comparison of output curves of the diode in the dark and under the illumination of 532 nm laser at $V_{DS} = 1V$ in a linear scale. And the inset shows in a logarithmic scale. c). Time-dependent photoresponse curves of the diode with 1 V bias voltage applied in forward and reverse directions. d) Band structure and carrier transport schematic of WS_2 p-n homojunction with forward bias (top) and reverse bias (bottom) under 532 nm laser. e) Photoswitching property at the photovoltaic mode under 650, 532, and 450 nm laser illumination. f) Photovoltaic switching characteristics of the homojunction phototransistor under 532 nm laser with different intensities. g) The time-resolved photoresponse of the homojunction photodiode in the photovoltaic mode under a 532 nm laser illumination. h,i) Power-dependent photocurrent (h), responsivity, and the detectivity (i) of the self-driven p-n homojunction phototransistor as a function of laser intensity. j) Stability testing of the self-driven WS_2 p-n homojunction phototransistor.

It is noteworthy that, in contrast to homojunction channels, both V-doped and pristine WS_2, when used as single materials for the phototransistor channel, lead to significantly larger dark currents (Figure S18, Supporting Information), leading to their comparatively weaker photoresponse switching ratio. This underscores the advantage of homojunction phototransistors for achieving low-power and highly sensitive detectors (Figures S19, S20, Supporting Information). More importantly, these homojunction devices can operate as self-powered photodetectors under zero bias, exhibiting exceptional photovoltaic properties. Figure 5e shows the time-resolved photovoltaic response under laser illumination at different wavelengths with similar power levels, where the photocurrent displays distinct and stable switching characteristics. Figure 5f and Figure S21 (Supporting Information) illustrate the time-resolved photovoltaic response under varying 532 nm laser illumination power intensities. Notably, under zero bias, the photocurrent shows a clear dependence on the incident laser intensity, with its magnitude achieving a high on/off current ratio of ≈10^3 under an intensity of 43.6 mW cm^{-2}. Furthermore, compared to similar TMDs heterojunction p-n photodiodes, the device achieves an even faster response time of ≈400 μs (Figure 5g), which can be attributed to the superior vdWs homojunction interface quality with excellent lattice matching.[18,48,49]

To further elucidate the mechanism of photocurrent generation in the photovoltaic mode, the power dependence of the photocurrent I_{ph} (defined as $I_{ph} = I_{light} - I_{dark}$) can be fitted using the power-law equation:

$$I_{ph} = AP^{\alpha} \tag{4}$$

where A is the scaling constant, α is the fitting exponent, and P represents the laser intensity. The fitting results reveal a power dependence of 0.99 for the photocurrent (Figure 5h), indicating

an almost linear relationship between photocurrent and light intensity. This suggests excellent photon-to-electron conversion efficiency, primarily driven by the photovoltaic effect dominating the photocurrent response in the WS_2-based p-n homojunction. Theoretically, forming a type-II band alignment and the high-quality homogeneous interface contributes to this linearity. As a result, photoexcited carriers are efficiently separated within the depletion region, minimizing accumulation or trapping at the interface. Moreover, the performance of the device can also be evaluated using photoresponsivity (R) and detectivity (D^*), which are key figures of merit defined as follows:

$$R = \frac{I_{ph}}{PS} \tag{5}$$

$$D^* = \mathrm{R}\sqrt{\frac{S}{2eI_{dark}}} \tag{6}$$

where S is the effective irradiated area (homojunction overlap area: 14×40 μm^2) and e is the electronic charge. Based on the above equations, the R and D^* dependence on laser intensity under zero bias is illustrated in Figure 5i. Remarkably, both parameters exhibit a decreasing trend as the laser intensity increases, which is primarily attributed to enhanced carrier recombination at higher power densities.[50–52] Under a low laser intensity of 2.2 mW cm^{-2}, the device achieves a favorable responsivity of 4.35 mA W^{-1} and an impressive specific detectivity of 3.32×10^{10} Jones. Furthermore, the WS_2 p-n homojunction phototransistor demonstrates outstanding stability when operated in self-powered photodetector mode (Figure 5j). Over a 900s laser on/off cycling test with a chopping frequency of 1 Hz, the device maintains consistent performance throughout. These findings evidently confirm its exceptional photovoltaic response performance and operational stability (Table S1, Supporting Information).

3. Conclusion

In conclusion, we successfully synthesized millimeter-scale monolayer V-doped WS_2 thin films as p-type channel materials using an atomic substitution doping strategy. By precisely aligning the band structure with the work function of the Ni electrodes, we achieved an ultra-low contact barrier of just 22 meV, enabling the fabrication of high-performance 2D p-type FETs with an exceptional current on/off ratio exceeding 10^6. Building on these advancements, we constructed quasi-ohmic contact p-type and n-type FET arrays based on tailored monolayer WS_2, which facilitated the development of WS_2 p-n vdWs homojunction phototransistor arrays. The homojunction phototransistor exhibits distinctive anti-ambipolar behavior, which arises from changes in series resistance induced by the gate voltage modulation. Meanwhile, the p-n homojunction operates as a photodiode, demonstrating excellent rectification characteristics and sub-picoampere dark current. In self-powered photodetection mode, the device achieves a photocurrent on/off ratio of ≈10^3, a high specific detectivity of 3.4×10^{10} Jones, and a fast response time of 400 μs, owing to the strong coupling and no dangling bonds nature of the van der Waals homojunction interface. These outstanding features emphasize the immense potential of WS_2-based p-n structures in advancing high-density data storage, powerful logic devices, and multifunctional optoelectronic systems by seamlessly integrating photodetection and logic functionalities, with promising prospects for large-scale industrial applications.

4. Experimental Section

Growth of Large-Size Monolayer Pristine or V-Doped WS_2 by CVD: The precursor solution, which provides the W and V atoms, was prepared by dissolving 0.1 g each of ammonium tungstate ($(NH_4)_6H_2W_{12}O_{40}\cdot xH_2O$, Aladdin) and ammonium vanadate (NH_4VO_3, Aladdin), along with 0.1 g of sodium hydroxide (NaOH, Aladdin) in 20 mL of deionized (DI) water, respectively. The resulting individual solutions were mixed with a saturated iodixanol ($C_{35}H_{44}I_6N_6O_{15}$, Aladdin) in a 1:1:1:1 volume ratio. This combination created a uniform and well-dispersed precursor solution with enhanced film-forming properties. SiO_2 (270 nm)/Si was first treated with oxygen plasma to prepare the substrates to improve surface cleanliness and enhance hydrophilicity. The prepared precursor solution was then spin-coated onto the treated SiO_2/Si substrates at 3000 rpm for 1 min. Then, the spin-coated substrates were placed in the downstream section of a dual-temperature CVD chamber. A quartz boat containing 100 mg of sulfur powder was positioned in the upstream section. After evacuating the CVD chamber and purging it with argon gas, the chamber pressure was stabilized at atmospheric levels. The upstream temperature gradually increased to 220 °C, and the downstream temperature was raised to 800 °C. The system was maintained at this temperature for 20 min to facilitate growth. Finally, the chamber was allowed to cool to room temperature naturally.

Characterization: Raman, PL spectroscopy, and spectral mapping were performed using a confocal microscope spectrometer (Alpha 300R, WITec, 532 nm laser, 2 mW power). X-ray photoelectron spectroscopy (XPS) was conducted using an ESCALAB XI+ X-ray Photoelectron Spectrometer (Thermo Fisher). The atomic structure and V atom doping ratio were determined through high-angle annular dark-field scanning transmission electron microscopy (HAADF-STEM, JEM-ARM300F2, JEOL, 80 kV). UV photoelectron spectroscopy (UPS) measurements were carried out using the ESCALAB XI+ X-ray Photoelectron Spectrometer with a He I resonance line (wavelength 584 Å, photon energy 21.22 eV) as the excitation source. The SEM images were characterized using the Thermo Fisher Apreo 2.

Patterning for Large-Size Monolayer V-Doped WS_2 Film: The SiO_2/Si substrate containing millimeter-sized monolayer V-doped WS_2 single-crystal films was cut to an appropriate size, and a uniform layer of photoresist (AZ5214) was spin-coated onto its surface at 5000 rpm for 1 min. The substrate was then baked at 110 °C for 1 min to cure the photoresist. Using a 390 nm laser, the desired array pattern was written onto the photoresist layer, followed by a development process to remove the exposed areas of the photoresist, leaving the array pattern areas covered while exposing the remaining regions. Subsequently, O_2 plasma etching (with a power of 80 W for 10 s) was applied to selectively remove material from the exposed regions of the substrate. Finally, the residual photoresist in the patterned areas was dissolved and removed, resulting in the desired patterned V-doped WS_2 thin film arrays.

Transfer Process of Arrayed Patterns for WS_2 p-n Homojunction: PMMA (495K, A6, Micro-Chem) was spin-coated uniformly onto the SiO_2/Si substrate with a patterned n-type pristine WS_2 array at 3000 rpm for 1 min, followed by baking at 180 °C for 1 min. The substrate was then immersed in a 1 mol L^{-1} NaOH solution at 70 °C until the PMMA film detached from the surface. The floating PMMA film was transferred to deionized water for rinsing to remove residual NaOH. Next, the PMMA film was carefully retrieved and aligned under a microscope onto the target substrate containing the patterned p-type V-doped WS_2 array, forming a WS_2 p-n homojunction array. The aligned substrate was then baked at 80 °C for 1 min to improve adhesion before being immersed in heated acetone to remove the PMMA film.

Device Fabrication and Measurements: To mitigate high gate leakage currents caused by pinholes and microcracks in the dielectric layer of the substrate during high-temperature CVD growth, all FET devices in this study were fabricated by transferring the channel materials from the growth substrates onto fresh SiO_2 (50 nm)/Si substrates before device assembly. The source/drain contact electrodes were defined using a standard laser direct writing process and constructed via evaporation. For p-type V-doped WS_2 devices, 50 nm Ni was used as the contact electrodes, while for n-type pristine WS_2 devices, the contact electrodes were composed of 5/45 nm Ti/Au. The deposition rate was consistently maintained relatively low to prevent potential damage to the channel material during the metal electrode deposition process (≈0.5 Å s^{-1}).

All electrical measurements were conducted under a bottom-gate configuration with two probes. For the analysis of the contact barrier height at the metal-semiconductor interface, the corresponding I_{DS}-V_{DS} and I_{DS}-V_{BG} curves were measured using a low-temperature probing station (Cryogenic Probe Stations LAKE SHORE CRX VF) in conjunction with an Agilent 4155C semiconductor parameter analyzer. All other room-temperature electronic characteristics were systematically evaluated using a standard electrical probe station under a dark or laser illumination environment, with the laser power accurately calibrated and measured using a power meter (PM400, Thorlabs). To capture high-resolution time response curves of the p-n homojunction photodiode, a digital oscilloscope (TBS 1102B-EDU, Tektronix) was employed in conjunction with a low-noise current preamplifier (SR570, Stanford Research Systems).

Supporting Information

Supporting Information is available from the Wiley Online Library or from the author.

Acknowledgements

The project was supported by the Innovation and Technology Fund (MHP/044/23) from the Innovation and Technology Commission of Hong Kong SAR, China, a fellowship award from the Research Grants Council of Hong Kong SAR, China (CityURFS2021-1S04), the Guangdong Basic and Applied Basic Research Fund (Project no. 2024A1515011922), the Shenzhen Municipality Science and Technology Innovation Commission (Project No. JCYJ20230807114910021), and the Shenzhen Research Institute, City University of Hong Kong.

Conflict of Interest

The authors declare no conflict of interest.

Data Availability Statement

The data that support the findings of this study are available from the corresponding author upon reasonable request.

Keywords

anti-ambipolar, doping, phototransistor, p-type, WS_2

Received: December 29, 2024
Revised: February 18, 2025
Published online:

[1] Y. Liu, X. Duan, H. J. Shin, S. Park, Y. Huang, X. Duan, *Nature* **2021**, *591*, 43.
[2] S. Wang, X. Liu, M. Xu, L. Liu, D. Yang, P. Zhou, *Nat. Mater.* **2022**, *21*, 1225.
[3] K. Zhu, C. Wen, A. A. Aljarb, F. Xue, X. Xu, V. Tung, X. Zhang, H. N. Alshareef, M. Lanza, *Nat. Electron.* **2021**, *4*, 775.
[4] J. Li, X. Yang, Y. Liu, B. Huang, R. Wu, Z. Zhang, B. Zhao, H. Ma, W. Dang, Z. Wei, K. Wang, Z. Lin, X. Yan, M. Sun, B. Li, X. Pan, J. Luo, G. Zhang, Y. Liu, Y. Huang, X. Duan, X. Duan, *Nature* **2020**, *579*, 368.
[5] A. K. Geim, I. V. Grigorieva, *Nature* **2013**, *499*, 419.
[6] R. Wu, Q. Tao, J. Li, W. Li, Y. Chen, Z. Lu, Z. Shu, B. Zhao, H. Ma, Z. Zhang, X. Yang, B. Li, H. Duan, L. Liao, Y. Liu, X. Duan, X. Duan, *Nat. Electron.* **2022**, *5*, 497.
[7] L. Tong, J. Wan, K. Xiao, J. Liu, J. Ma, X. Guo, L. Zhou, X. Chen, Y. Xia, S. Dai, Z. Xu, W. Bao, P. Zhou, *Nat. Electron.* **2023**, *6*, 37.
[8] D. Li, M. Chen, Z. Sun, P. Yu, Z. Liu, P. M. Ajayan, Z. Zhang, *Nat. Nanotechnol.* **2017**, *12*, 901.
[9] L. Wu, A. Wang, J. Shi, J. Yan, Z. Zhou, C. Bian, J. Ma, R. Ma, H. Liu, J. Chen, Y. Huang, W. Zhou, L. Bao, M. Ouyang, S. J. Pennycook, S. T. Pantelides, H. J. Gao, *Nat. Nanotechnol.* **2021**, *16*, 882.
[10] Y. Meng, W. Wang, W. Wang, B. Li, Y. Zhang, J. Ho, *Adv. Mater.* **2024**, *36*, 2306290.
[11] C. R. Paul Inbaraj, R. J. Mathew, R. K. Ulaganathan, R. Sankar, M. Kataria, H. Y. Lin, Y. T. Chen, M. Hofmann, C. H. Lee, Y. F. Chen, *ACS Nano* **2021**, *15*, 8686.
[12] D. Jariwala, V. K. Sangwan, C. C. Wu, P. L. Prabhumirashi, M. L. Geier, T. J. Marks, L. J. Lauhon, M. C. Hersam, *Proc. Natl. Acad. Sci. USA* **2013**, *110*, 18076.
[13] S. B. Jo, J. Kang, J. H. Cho, *Adv. Sci. (Weinh)* **2021**, *8*, 2004216.
[14] J. Kim, M. Jung, D. U. Lim, D. Rhee, S. H. Jung, H. K. Cho, H. K. Kim, J. H. Cho, J. Kang, *Nano Lett.* **2022**, *22*, 570.
[15] M. E. Beck, A. Shylendra, V. K. Sangwan, S. Guo, W. A. Gaviria Rojas, H. Yoo, H. Bergeron, K. Su, A. R. Trivedi, M. C. Hersam, *Nat. Commun.* **2020**, *11*, 1565.
[16] W. Wang, W. Wang, Y. Meng, Q. Quan, Z. Lai, D. Li, P. Xie, S. Yip, X. Kang, X. Bu, D. Chen, C. Liu, J. C. Ho, *ACS Nano* **2022**, *16*, 11036.
[17] Y. Wakayama, R. Hayakawa, *Adv. Funct. Mater.* **2019**, *30*, 1903724.
[18] E. Wu, Y. Xie, Q. Liu, X. Hu, J. Liu, D. Zhang, C. Zhou, *ACS Nano* **2019**, *13*, 5430.
[19] H. Ning, Z. Yu, T. Li, H. Shen, G. Long, Y. Shi, X. Wang, *Sci. China Info. Sci.* **2023**, *66*, 160411.
[20] S. S. Sylvia, K. Alam, R. K. Lake, *IEEE J. Exp. Solid-State Comput. Dev. Circ.* **2016**, *2*, 28.
[21] Q. He, Y. Liu, C. Tan, W. Zhai, G. H. Nam, H. Zhang, *ACS Nano* **2019**, *13*, 12294.
[22] Y. Shen, Z. Dong, Y. Sun, H. Guo, F. Wu, X. Li, J. Tang, J. Liu, X. Wu, H. Tian, T. L. Ren, *Adv. Mater.* **2022**, *34*, 2201916.
[23] Y. Pan, T. Jian, P. Gu, Y. Song, Q. Wang, B. Han, Y. Ran, Z. Pan, Y. Li, W. Xu, P. Gao, C. Zhang, J. He, X. Xu, Y. Ye, *Nat. Commun.* **2024**, *15*, 9631.
[24] M. Das, D. Sen, N. U. Sakib, H. Ravichandran, Y. Sun, Z. Zhang, S. Ghosh, P. Venkatram, S. Subbulakshmi Radhakrishnan, A. Sredenschek, Z. Yu, K. J. Sarkar, M. U. K. Sadaf, K. Meganathan, A. Pannone, Y. Han, D. E. Sanchez, D. Somvanshi, Z. Sofer, M. Terrones, Y. Yang, S. Das, *Nat. Electron.* **2024**, *8*, 24.
[25] Y. C. Lin, R. Torsi, D. B. Geohegan, J. A. Robinson, K. Xiao, *Adv. Sci. (Weinh)* **2021**, *8*, 2004249.
[26] S. Li, J. Hong, B. Gao, Y. C. Lin, H. E. Lim, X. Lu, J. Wu, S. Liu, Y. Tateyama, Y. Sakuma, K. Tsukagoshi, K. Suenaga, T. Taniguchi, *Adv. Sci. (Weinh)* **2021**, *8*, 2004438.
[27] F. Zhang, Y. Lu, D. S. Schulman, T. Zhang, K. Fujisawa, Z. Lin, Y. Lei, A. L. Elias, S. Das, S. B. Sinnott, M. Terrones, *Sci. Adv.* **2019**, *5*, eaav5003.
[28] A. Azcatl, X. Qin, A. Prakash, C. Zhang, L. Cheng, Q. Wang, N. Lu, M. J. Kim, J. Kim, K. Cho, R. Addou, C. L. Hinkle, J. Appenzeller, R. M. Wallace, *Nano Lett.* **2016**, *16*, 5437.

[29] B. S. Y. Kim, T. D. Ngo, Y. Hassan, S. H. Chae, S. G. Yoon, M. S. Choi, *Adv. Sci. (Weinh)* **2024**, *11*, 2407175.
[30] J. Tang, Z. Wei, Q. Wang, Y. Wang, B. Han, X. Li, B. Huang, M. Liao, J. Liu, N. Li, Y. Zhao, C. Shen, Y. Guo, X. Bai, P. Gao, W. Yang, L. Chen, K. Wu, R. Yang, D. Shi, G. Zhang, *Small* **2020**, *16*, 2004276.
[31] S. Das, A. Sebastian, E. Pop, C. J. McClellan, A. D. Franklin, T. Grasser, T. Knobloch, Y. Illarionov, A. V. Penumatcha, J. Appenzeller, Z. Chen, W. Zhu, I. Asselberghs, L.-J. Li, U. E. Avci, N. Bhat, T. D. Anthopoulos, R. Singh, *Nat. Electron.* **2021**, *4*, 786.
[32] Y. Wang, S. Sarkar, H. Yan, M. Chhowalla, *Nat. Electron.* **2024**, *7*, 638.
[33] B. Gao, W. Wang, Y. Meng, C. Du, Y. Long, Y. Zhang, H. Shao, Z. Lai, W. Wang, P. Xie, S. Yip, X. Zhong, J. C. Ho, *Small* **2024**, *20*, 2402217.
[34] J. Zou, Z. Cai, Y. Lai, J. Tan, R. Zhang, S. Feng, G. Wang, J. Lin, B. Liu, H. M. Cheng, *ACS Nano* **2021**, *15*, 7340.
[35] S. J. Yun, D. L. Duong, D. M. Ha, K. Singh, T. L. Phan, W. Choi, Y. M. Kim, Y. H. Lee, *Adv. Sci. (Weinh)* **2020**, *7*, 1903076.
[36] F. Zhang, B. Zheng, A. Sebastian, D. H. Olson, M. Liu, K. Fujisawa, Y. T. H. Pham, V. O. Jimenez, V. Kalappattil, L. Miao, T. Zhang, R. Pendurthi, Y. Lei, A. L. Elias, Y. Wang, N. Alem, P. E. Hopkins, S. Das, V. H. Crespi, M. H. Phan, M. Terrones, *Adv. Sci. (Weinh)* **2020**, *7*, 2001174.
[37] L. Tang, R. Xu, J. Tan, Y. Luo, J. Zou, Z. Zhang, R. Zhang, Y. Zhao, J. Lin, X. Zou, B. Liu, H. M. Cheng, *Adv. Funct. Mater.* **2020**, *31*, 2006941.
[38] K. Schauble, D. Zakhidov, E. Yalon, S. Deshmukh, R. W. Grady, K. A. Cooley, C. J. McClellan, S. Vaziri, D. Passarello, S. E. Mohney, M. F. Toney, A. K. Sood, A. Salleo, E. Pop, *ACS Nano* **2020**, *14*, 14798.
[39] R. T. Tung, *Appl. Phys. Rev.* **2014**, *1*, 011304.
[40] X. Liu, M. S. Choi, E. Hwang, W. J. Yoo, J. Sun, *Adv. Mater.* **2022**, *34*, 2108425.
[41] K. Sotthewes, R. van Bremen, E. Dollekamp, T. Boulogne, K. Nowakowski, D. Kas, H. J. W. Zandvliet, P. Bampoulis, *J. Phys. Chem. C Nanomater. Interfaces* **2019**, *123*, 5411.
[42] P. C. Shen, C. Su, Y. Lin, A. S. Chou, C. C. Cheng, J. H. Park, M. H. Chiu, A. Y. Lu, H. L. Tang, M. M. Tavakoli, G. Pitner, X. Ji, Z. Cai, N. Mao, J. Wang, V. Tung, J. Li, J. Bokor, A. Zettl, C. I. Wu, T. Palacios, L. J. Li, J. Kong, *Nature* **2021**, *593*, 211.
[43] J. R. Chen, P. M. Odenthal, A. G. Swartz, G. C. Floyd, H. Wen, K. Y. Luo, R. K. Kawakami, *Nano Lett.* **2013**, *13*, 3106.
[44] A. Allain, J. Kang, K. Banerjee, A. Kis, *Nat. Mater.* **2015**, *14*, 1195.
[45] H. H. Choi, K. Cho, C. D. Frisbie, H. Sirringhaus, V. Podzorov, *Nat. Mater.* **2017**, *17*, 2.
[46] Y. Jiang, W. Xing, H. Li, L. Zhang, S. Zhang, X. Li, J. Su, X. Song, C. Xia, *Appl. Phys. Lett.* **2022**, *121*, 022101.
[47] J. Leveillee, X. Zhang, E. Kioupakis, F. Giustino, *Phys. Rev. B* **2023**, *107*, 125207.
[48] Z. Zou, J. Liang, X. Zhang, C. Ma, P. Xu, X. Yang, Z. Zeng, X. Sun, C. Zhu, D. Liang, X. Zhuang, D. Li, A. Pan, *ACS Nano* **2021**, *15*, 10039.
[49] J. You, Z. Jin, Y. Li, T. Kang, K. Zhang, W. Wang, M. Xu, Z. Gao, J. Wang, J. K. Kim, Z. Luo, *Adv. Funct. Mater.* **2024**, *34*, 2311134.
[50] L. H. Zeng, S. H. Lin, Z. J. Li, Z. X. Zhang, T. F. Zhang, C. Xie, C. H. Mak, Y. Chai, S. P. Lau, L. B. Luo, Y. H. Tsang, *Adv. Funct. Mater.* **2018**, *28*, 1705970.
[51] G. Konstantatos, I. Howard, A. Fischer, S. Hoogland, J. Clifford, E. Klem, L. Levina, E. H. Sargent, *Nature* **2006**, *442*, 180.
[52] W. Y. Kong, G. A. Wu, K. Y. Wang, T. F. Zhang, Y. F. Zou, D. D. Wang, L. B. Luo, *Adv. Mater.* **2016**, *28*, 10725.